Research Article Vol. 37, No. 9 / September 2020 / Journal of the Optical Society of America A B93

Journal of the Optical Society of America A

OPTICS, IMAGE SCIENCE, AND VISION

Multi-view fringe projection system for surface topography measurement during metal powder bed fusion

ANDREW DICKINS,[1,*] TAUFIQ WIDJANARKO,[1] DANNY SIMS-WATERHOUSE,[2] ADAM THOMPSON,[1] SIMON LAWES,[1] NICOLA SENIN,[1,3] AND RICHARD LEACH[1,2]

[1]Manufacturing Metrology Team, Faculty of Engineering, University of Nottingham, Nottingham, UK
[2]Taraz Metrology, Nottingham, UK
[3]Department of Engineering, University of Perugia, Perugia, Italy
*Corresponding author: andrew.dickins@nottingham.ac.uk

Received 29 April 2020; revised 26 June 2020; accepted 29 June 2020; posted 30 June 2020 (Doc. ID 396186); published 19 August 2020

Metal powder bed fusion (PBF) methods need in-process measurement methods to increase user confidence and encourage further adoption in high-value manufacturing sectors. In this paper, a novel measurement method for PBF systems is proposed that uses multi-view fringe projection to acquire high-resolution surface topography information of the powder bed. Measurements were made using a mock-up of a commercial PBF system to assess the system's accuracy and precision in comparison to conventional single-view fringe projection techniques for the same application. Results show that the multi-view system is more accurate, but less precise, than single-view fringe projection on a point-by-point basis. The multi-view system also achieves a high degree of surface coverage by using alternate views to access areas not measured by a single camera.

https://doi.org/10.1364/JOSAA.396186

1. INTRODUCTION

Additive manufacturing (AM) is an increasingly important production route for a number of industrial sectors and continues to see rapid growth [1]. Those working in high-value sectors, such as aerospace, automotive, and biomedical manufacturing, have a strong interest in metal AM methods, such as metal powder bed fusion (PBF), due to the added geometrical complexity, component functionality, and bespoke design capabilities when compared to conventional manufacturing methods, such as milling or turning. However, the layer by layer building process and high energy input of the laser in metal PBF make for a complex and poorly understood process, which causes a lack of confidence in the quality of parts being built [2,3]. A significant cause for the lack of confidence in additive components stems from a lack of understanding of the physical phenomena present during the build process [3–6], as well as cost concerns associated with wasted time and discarded raw materials when a build process fails [3,7–9]. On-machine metrology has been of interest in recent years for both process monitoring and defect detection, to further understand the mechanics of the PBF process. This growing interest has encouraged the development of on-machine measurement solutions [4–6,10].

Reviews covering previous AM monitoring research and further requirements for future systems have been published by Everton *et al.* [11], Mani *et al.* [12], and Grasso and Colosimo [13]. On-machine measurement solutions that have been developed include co-axial [10,14–25] and off-axis [4–6,26–30] melt pool monitoring systems, as well as thermal [31–33] and optical [23,34–37] imaging of the powder bed. The target of these in-process monitoring systems is to detect defective regions of the powder bed, to inform the user that the component being built may require either corrective action or termination. Several research systems now have machine learning implemented to find correlations between observed signals and defective surface phenomenon [19,20,22,24,36,37]. Other options for in-process monitoring aim to acquire height information of the powder bed surface through either mounting a line scanner on the recoater blade [38,39] or using digital fringe projection techniques [40–46] which provide topographical information of surface features that cannot be obtained through melt pool monitoring or simple imaging methods.

Fringe projection is an optical measurement method commonly used for the three-dimensional measurement of object form and is used in many sectors due to its relatively fast acquisition rates and non-destructive nature [47–50]. In their simplest

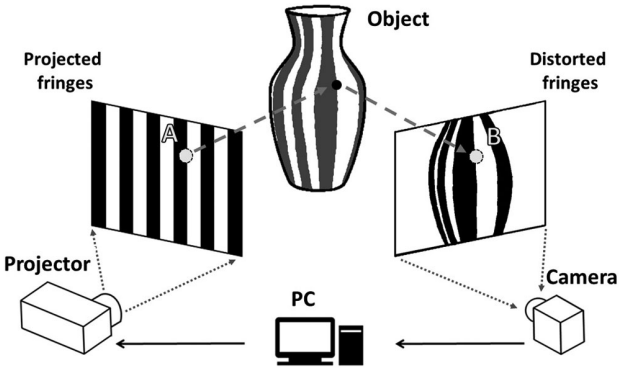

Fig. 1. Illustration of depth determination in fringe projection. Points A and B mark the same point on the measured object through both the projector's and camera's perspectives.

form, fringe projection systems consist of a single camera–projector pair, sharing a common field of view (FoV) that acts as the measurement volume. Fringe images from the projector are distorted by the object's shape and, when viewed from a different perspective by the camera, these distortions can be used to reconstruct the shape of the object, as shown in Fig. 1. Depth information can be derived from the distortion of the fringes, making it possible to calculate the form of an object through a series of image projections and captures. The rapid acquisition rate and non-contact nature of fringe projection make it appealing as an in-process measurement tool. However, fringe projection has several disadvantages. When measuring highly specular surfaces, as would be expected during the AM build process of a metal component, data quality decreases and data drop-out occurs when the positional value cannot be resolved [49]. In addition to data drop-out issues, there is an inherent trade-off between the system's FoV and the resolving power of a given camera sensor, meaning that obtaining a measurement of the complete powder bed region often requires the sacrifice of smaller-scale surface details due to an effective decrease in magnification [51]. To combat issues such as data drop-out or surface occlusions due to part form, fringe projection systems often use multi-view approaches that allow multiple measurements to be taken from different viewing points. Typically, the capture of multiple views is performed by placing the part being measured on a rotary table and performing a measurement at fixed angles [52–54] or by mounting the fringe projection system onto a robot arm to be moved around the part [55,56]. Other methods have focused on the simultaneous capture of multiple views by introducing more camera–projector pairs [57–59]. Simultaneous capture is beneficial as no moving parts are required and the capture time can be greatly reduced when compared to rotation stage or robot arm methods. However, when using a simultaneous capture approach with multiple cameras, limitations in the flexibility of the system are introduced.

The rapid acquisition and non-contact nature of fringe projection makes the method ideal for performing in-process topographic measurements without significantly interrupting the build process. Multiple in-process monitoring systems have been proposed for PBF systems which the target of detecting defects that have arisen on the build area through topographical analysis of the powder bed.

Land *et al.* [40] and Zhang *et al.* [41] present work on a single camera–projector pair fringe projection system for use in a custom-built metal laser PBF (L-PBF) machine. The system consisted of a DSLR camera (pixel array: 5184 × 3456) that measured approximately (100 × 100) mm of the build plate. This system proved capable of recognizing regions of sintered material due to the elevation drop from the powder layer. Zhang *et al.* [42] later reconfigured the system using a machine vision camera (pixel array: 4096 × 2160) which covered a reduced FoV of (28 × 15) mm. In this configuration, a lateral point spacing of 6.8 μm was achieved with a single point repeatability of 0.47 μm. This higher lateral resolution was achieved by trading off the larger FoV, making the system less beneficial for full powder bed process monitoring, but still highlighting fringe projection as a valuable tool for in-process high-resolution measurement. Li *et al.* [43] applied a two-camera, single-projector fringe projection setup to a metal L-PBF system capable of identifying sintered contours. For this work, two machine vision cameras (pixel array: 2592 × 1944) were used to measure a region of the powder bed approximately (200 × 250) mm in size. Resolving capabilities were not discussed, but regions of the powder that had dropped from the nominal plane were identifiable. Southon *et al.* [44] investigated the use of a commercial fringe projection system pointed through the viewing window of a commercial polymer L-PBF machine as an in-process monitoring system. Over a measured region of approximately (200 × 100) mm, curling defects were identified on the test part being observed, with height differences as low as 50 μm being clearly visible in the data. Liu *et al.* used the fringe projection method and applied it to an electron beam (EB-PBF) system [45,46]. In this method a single camera and projector pair (pixel arrays of 3016 × 4016 and 912 × 1140, respectively) was used to observe a region of approximately (90 × 90) mm on the powder bed. A measurement of 24 fringes was taken in approximately 2 s. This system implemented an active feedback loop that either respreads the powder or alters the process parameters for correction when an issue is identified. The system was typically found to measure vertical distances to within 7 μm when compared to a laser interferometer displacement measurement with the accuracy of the system quoted to be 15.8 μm.

From these publications, fringe projection methods have been demonstrated to have potential for in-process monitoring of AM systems. However, improvements need to be made to achieve a higher-resolution surface reconstruction that can be used for feature-based identification of defects [60–63] that are sub-100 μm in lateral size. A feature-based identification approach could provide a more robust method of determining the successful manufacture of each additive layer and, therefore, the whole component.

In this paper, a multi-view fringe projection system is proposed for novel in-process monitoring of PBF machines. The aim of the system is to maintain a high resolving power over the entire powder bed area, that is capable of measuring PBF surface features and defects, by combining multiple measurements from four different cameras. Using multiple views to measure the same surface also reduces regions of data dropout (if, when data dropout occurs in one camera, one of the other views is able to measure it). Using multiple views to acquire four point clouds should also increase user confidence in the measurements as a

metric for data quality could be calculated based on how well the four point clouds agree on the surface reconstruction. Results are presented from a prototype PBF chamber to compare the performance differences between a single and novel, in-house multi-view fringe projection system for on-machine monitoring applications.

2. METHODOLOGY

A. Measurement Technologies

To test the proposed multi-view fringe projection system, measurements were made of the same samples using the fringe projection system in its multi-view and single-view modes. Focus variation (FV) measurements were also taken of the samples to compare the fringe projection measurements against a higher-resolution system.

1. Fringe Projection

The multi-view fringe projection system is a four-camera, single-projector system that functions as four camera–projector pairs to perform a measurement. The system is comprised of four Basler ace acA572–17 um cameras [pixel array: 5472 × 3648, sensor size: (13.1 × 8.8) mm, maximum frame rate: 17 fps], each fitted with a MVL16M1 16 mm focal length lens, and an Optoma UHD550X projector (pixel array: 3840 × 2160, maximum frame rate: 24 fps, brightness: 2800 lm) fitted with a close-up lens attachment. The optics were chosen and configured to ensure that the systems resolution capabilities are sensor limited rather than optically limited. Components were arranged to replicate the space limitations presented by a Renishaw AM250, with a (265 × 265) mm measurement stage mimicking the build plate's size and location. The camera positions within the system are believed to be the most suitable for integration into a real PBF system without obstructing the laser optics. Images of the bench-top setup can be seen in Fig. 2. The fringe projection system is an updated version of the design described in Dickins *et al.* [64], specifically designed to be fitted into real AM systems to perform in-process monitoring of the powder bed on a layer by layer basis, and is being commercialized by Taraz Metrology Ltd.

Geometric characterization of the system was performed using a calibrated chequerboard which was placed manually in multiple locations around the measurement volume [58]. The geometric characterization accounts for non-linear distortion effects introduced by the cameras, but not the projector optics. The non-linear distortion introduced by the projector was deemed negligible for the FoV analyzed in this paper but is a priority for future improvements to the characterization process. Images were captured in each position, both with and without fringe projections, to acquire the intrinsic and extrinsic parameters of all four cameras and the projector within a common global reference frame. The fringe projection method used relies on a temporal phase unwrapping method that uses both phase-stepped sinusoidal fringes and varying frequency binary fringes to retrieve the absolute phase map. Further details of the geometric characterization and the fringe projection phase unwrapping methods are discussed in Shaheen *et al.* [58].

Nineteen images were captured per camera per measurement (eight binary images, 10 sinusoidal images, and a single white image). The number of phase steps used was chosen to minimize acquisition time while maintaining a high enough accuracy of measurement. The system operated as four separate camera–projector pairs, each outputting a point cloud of the measured surface. The four point clouds saved from a measurement cycle were initially coarsely aligned (due to the common reference frame), but required a further fine alignment process to create a combined, multi-view dataset (described in Section 2.C.1). The projection covers the entire width and most of the length (approximately 190 mm) of the (265 × 265) mm measurement stage with the FoV of all four cameras covering the entire projected image. Point clouds were acquired with both samples (described in Section 2.B) in the same measurement volume.

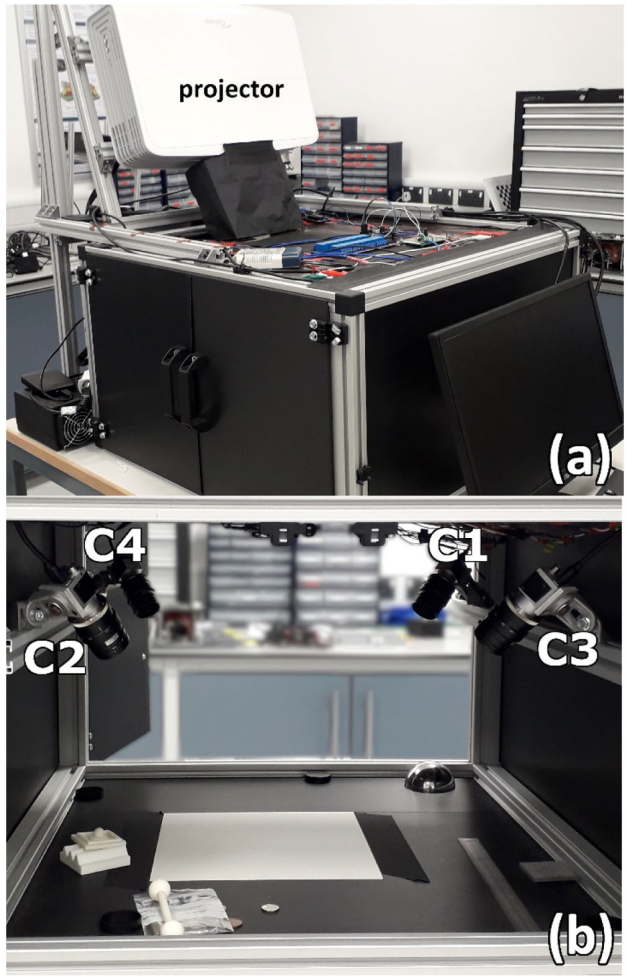

Fig. 2. Multi-view fringe projection system. (a) External view of fringe projection system with projector labeled. (b) Inside measurement chamber with the mock powder bed region (250 mm × 250 mm) and four cameras (labeled C1 to C4).

2. Focus Variation Microscopy

The fringe projection results were compared against those from a commercial FV system [65]. The FV system has well-quantified metrological characteristics [66,67] and its resolving power is orders of magnitude higher than that of the fringe projection system. The FV was used to measure the entire top surface of both samples using the following setup:

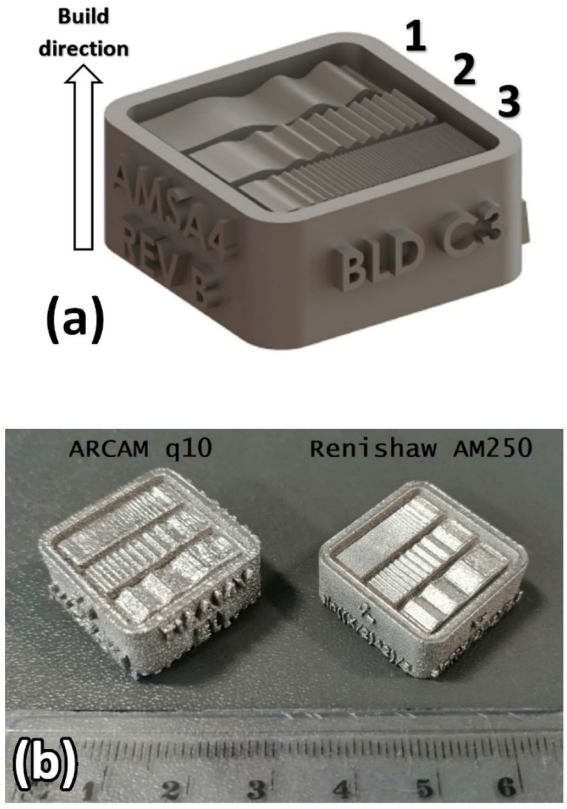

Fig. 3. (a) CAD model of the AMSA4 (modified from Townsend *et al.* [68]) with three sections labeled in correspondence to Table 1. (b) Photograph of the two AMSA4 samples, manufactured using EB-PBF (left) and L-PBF (right) against a ruler for scale (numbered divisions in centimeters).

5× magnification objective lens [numerical aperture: 0.15, FoV: (2.82 × 2.82) mm, pixel sampling resolution: 3.52 μm], coaxial illumination, measured area: (25 × 25) mm, stitching of multiple FoVs performed in the manufacturer's software. Height maps of the two samples from the FV system were acquired separately for each sample due to the FoV limitations of the FV system.

B. Samples

Two AM surface samples that were designed and manufactured by Townsend *et al.* using an ARCAM Q10 EB-PBF system and a Renishaw AM250 L-PBF system [68] were used as samples for all measurements. The ASMA4 samples include three sections, each with a constant amplitude and decreasing wavelength sine-wave structure along the section length. Both samples were manufactured with the measured plane of the structured surface orthogonal to the build direction (see Fig. 3).

For all measurements, the region of interest (RoI) was the top surfaces of the three 17 mm × 5 mm structured sections. The equations for the nominal structure of each section are given in Table 1, with the accuracy achieved in the manufacturing of the samples reported in Townsend *et al.* [68]. All data presented is exclusively of the three structured top sections.

Table 1. Equations of the CAD Models for the Three Structured Sections of the AMSA4 [68], Labeled in Fig. 3(a), Where *Y* Is the Amplitude and *X* Is the Distance along the Section in Millimeters

Section Number	Structure Equation/mm
1	$Y = 0.4\sin(\frac{X^2}{16})$
2	$Y = 0.2\sin(\frac{X^2}{4})$
3	$Y = 0.1\sin(X^2)$

C. Data Processing

The raw data output from the fringe projection and FV systems are point clouds (i.e., a 3D set of data points in space) and height maps (i.e., a collection of equispaced height points on a planar grid) formats respectively, with the fringe projection FoV being multiple times larger than that of the FV system. To allow meaningful comparison, the two datasets were both cropped to only include the top surface of the ASMA4, and the fringe projection data were converted to height maps (see Section 2.C.3). Five repeat measurements were made on the single- and multi-view fringe projection systems and the FV system without repositioning the sample, so that a statistical measure of repeatability could be estimated. A schema of the data processing pipeline is shown in Fig. 4 and detailed explanations of this pipeline follow throughout this section. Sample positioning within the fringe projection system is shown in Fig. 5.

1. Fringe Projection Data

The point cloud generated from each camera was imported into CloudCompare 3D point cloud processing software [69], where it was cropped to the region of the samples. A statistical outlier removal filter was applied (settings: number of points used for mean distance estimation = 8, standard deviations multiplier threshold $(n\sigma) = 1$, maximum point-to-point distance = mean distance + ($n\sigma$ × standard deviation). Following the cropping and noise removal process, the point cloud was exported as an ASCII text file.

Each point cloud was imported into Polyworks|Inspector [70], where they were further manually cropped to the RoI. A two-phase alignment process (coarse and fine) was performed to align the fringe projection point clouds to the FV measurements. The coarse alignment involved the manual selection of three common features between the target dataset (fringe projection point cloud) and the reference data (FV triangulated mesh). After the coarse alignment, a fine alignment was performed using an iterative closest point fitting algorithm [71,72]. During alignment, repeat measurements acquired using the same camera were fixed in space relative to one another to ensure that repeatability calculations were not influenced by geometric transformations. The multi-view point cloud was constructed by fusing the independent point clouds of each camera into a single high-density dataset. All datasets of the RoI are exported in an ASCII text point cloud format, before being converted to a triangulated mesh in Polyworks|Inspector through a Delaunay triangulation algorithm [73] with a maximum edge length of 0.7 mm. The polygonal models were all exported in ".ply" format.

The ASCII point clouds of the fringe projection RoIs are imported back into CloudCompare, where an approximate mean point spacing is calculated.

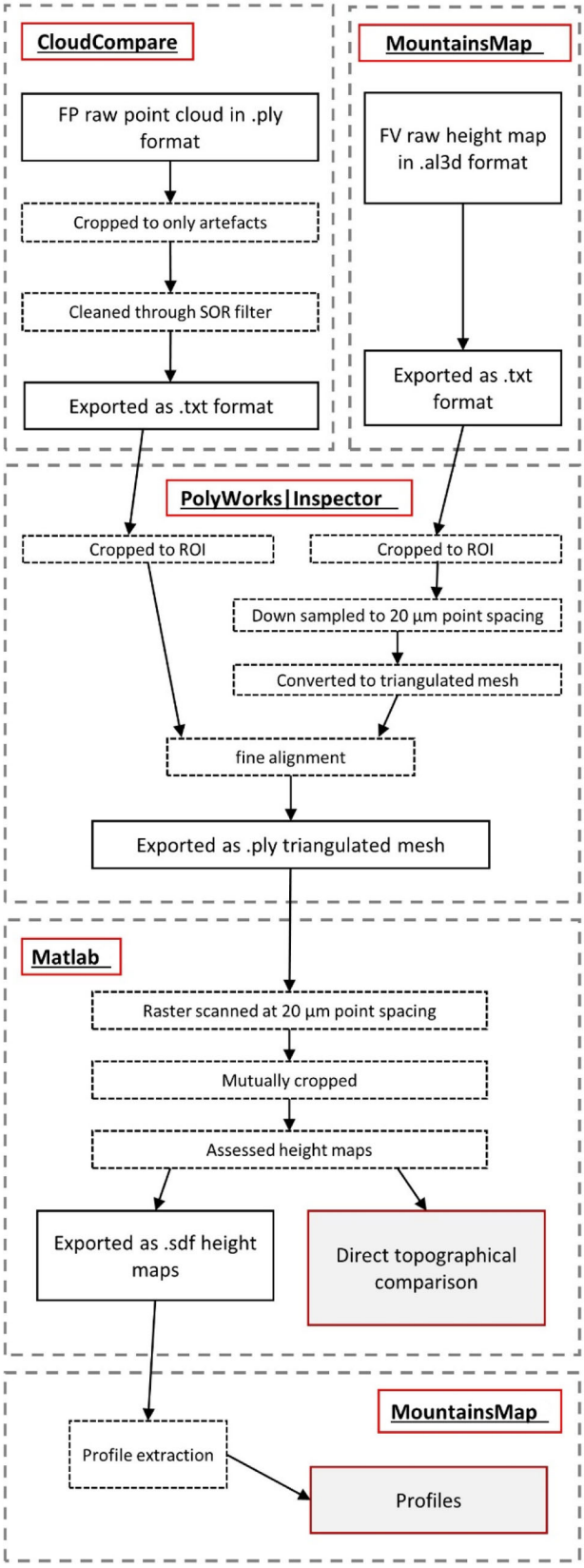

Fig. 4. Data processing pipeline for both fringe projection and FV measurements.

2. Focus Variation Data

Height maps from the FV system were imported into Polyworks|Inspector, downsampled to a 20 µm point spacing through linear interpolation, and converted into triangulated meshes using the same method outlined for the fringe projection point clouds in Section 2.C.1. Downsampling of the focus variation data at this stage was an unfortunate necessity as the computational load of aligning the high-resolution data in Polyworks|Inspector was beyond the capacity of the high-spec computers used.

3. Dataset Comparisons

A recently developed method [74] of point-by-point topography comparison that creates equipoint-spaced height maps of pre-aligned triangulated meshes was used for the fringe projection and FV datasets to be compared in a meaningful manner. Polygonal models of both samples are converted into height maps by virtual raster scanning [74–76] with a 20 µm point spacing. The height maps are equivalently cropped before a mean z-value for each measurement point is calculated with a corresponding 95% confidence interval (CI), providing a measure of the measurement precision.

Point-by-point deviations in height between the fringe projection and FV were mapped and the mean absolute deviation over the surface was calculated to provide a mean deviation which functions as a measure of the measurement accuracy (under the assumption that the FV measurement is a reference representation of the surface). Discrepancies between measurement methods are also mapped to present where the different methods disagree on the height position of each point. Discrepancy is defined here as the negative output from a binary measure that states where the CI width of the fringe projection and FV height values do or do not overlap with one another; therefore, its value is dependent on both the magnitude of deviation and the CI width. Discrepancy as a percentage over the surface provides a measure of how well two measurement methods agree with one another.

Surface coverage was calculated as the percentage of the FV surface measurement that the fringe projection measurements were able to provide data for. Calculations were performed using the final height map form of the measurement. The surface

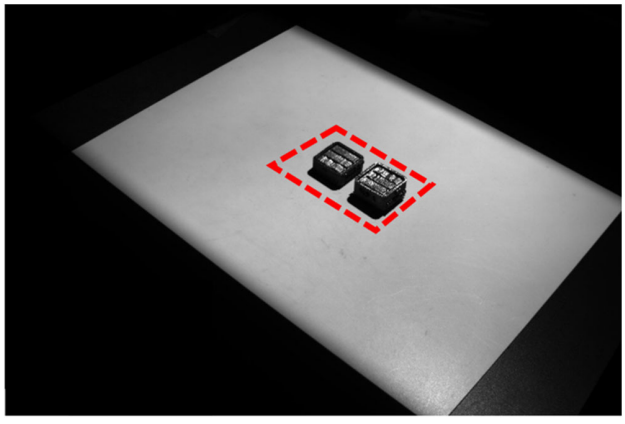

Fig. 5. White image of both AMSA4 samples within the measurement volume of the fringe projection system from the perspective of camera 1. The red box marks the region of initial cropping.

coverage values are used to provide a measure of data dropout on the fringe projection measurements and are calculated under the assumption that any data dropout on the FV measurement in negligible. The percentages calculated for this paper are also impacted by the minimum distance parameter used for the generation of the triangulated mesh. Although a change in the minimum edge length of the mesh would cause different values, the percentages can still be used as a qualitative measure of the surface coverage achieved.

Point spacings of the multi-view and single-view fringe projection point clouds are compared to act as an indicator of the system's potential resolving capabilities. It is understood that the point spacing is not synonymous with resolution. However, assuming that the alignment between the point clouds is sufficiently accurate and the system's resolving capability is not optically limited, the increase in point density would mean that a higher sampling rate is achieved over potential surface features which might not have been detectable otherwise.

Profiles were extracted along the center of each structured section from the aligned datasets using MountainsMap [77]. The profiles serve as a visual representation of the surface form that outline some effects of using multi-view over single-view fringe projection.

3. RESULTS AND DISCUSSION

A. Focus Variation Measurements

Height maps and associated CI widths of the FV measurements are presented in Fig. 6 for both L-PBF and EB-PBF samples. Mean CI widths for the FV measurements were calculated

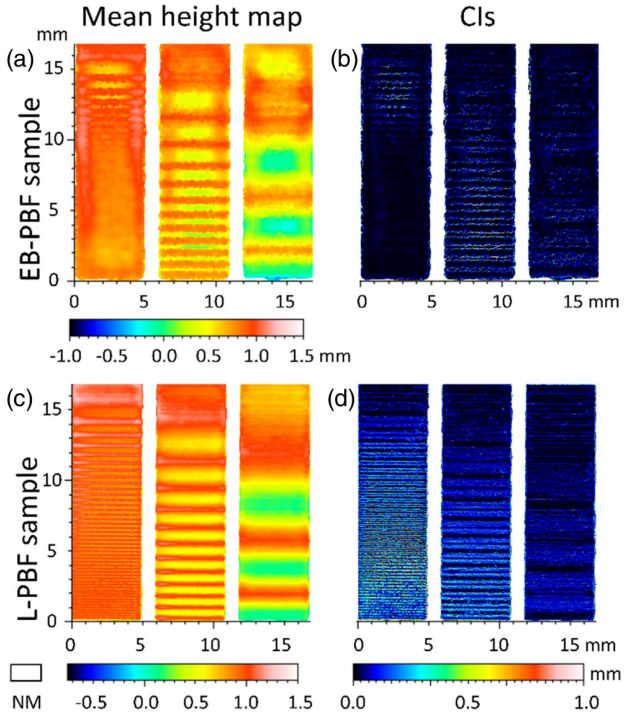

Fig. 6. (a),(c) Mean height maps and (b),(d) CI maps for the FV measurements of both the EB-PBF and L-PBF samples. Both CI plots are set to the same color bar; all saturated values exceed the color bar scale.

to be 10 μm and 27 μm for the EB-PBF and L-PBF samples, respectively. The higher mean CI width value for the L-PBF sample is likely a result of the high slope angles as the structured surface tends toward the highest spatial frequencies, which FV is known to have difficulty measuring [78]. On the EB-PBF sample, these high aspect ratio features are not present due to the manufacturing resolution limits of the EB-PBF system.

B. Fringe Projection Measurements

1. Surface Coverage

To assess the impact on data dropout over the measured surface, a percentage of surface overlap between the fringe projection and FV datasets is calculated (values presented in Tables 2 and 3). For both samples, the percentage of overlap on the measured surfaces is higher when multi-view is used, with some single-view measurements losing over 10% of the overall surface data. Height maps presented in Figs. 7 and 8 of the fringe projection data have regions of missing data from all individual cameras that are much less prevalent in the multi-view reconstruction. Although there are cases where a single-view perspective covers the majority of the surface, achieving surface coverage of up to 97.9%, the multi-view system still improves upon this, covering 99.5% of the surface for the same sample (L-PBF sample). High coverage of the single-view method is also

Table 2. Discrepancy (Percentage Point-by-Point Disagreement), Surface Overlap (Percentage of Data Surface Coverage), and Mean Deviation (Point-by-Point Difference in Height Value) between Fringe Projection and Focus Variation Height Maps of the EB-PBF Sample

	Multi-View Fringe	Single-View Fringe Projection			
EB-PBF Dataset	Projection	Cam1	Cam2	Cam3	Cam4
Discrepancy from FV/%	51.1	81.7	83.8	81.5	78.1
Surface overlap from FV/%	98.7	97.5	88.3	93.0	90.6
Mean deviation from FV/μm	67	83	92	77	81

Table 3. Discrepancy (Percentage Point-by-Point Disagreement), Surface Overlap (Percentage of Data Surface Coverage), and Mean Deviation (Point-by-Point Difference in Height Value) between Fringe Projection and Focus Variation Height Maps of the L-PBF Sample

	Multi-View Fringe	Single-View Fringe Projection			
L-PBF Dataset	Projection	Cam1	Cam2	Cam3	Cam4
Discrepancy from FV/%	49.9	78.9	75.4	78.2	73.2
Surface overlap from FV/%	99.5	97.9	90.3	97.8	88.2
Mean deviation from FV/μm	69	93	85	79	82

not consistent across the entire measurement volume. In measurements from camera 3, where 97.8% surface coverage was achieved of the L-PBF sample, the same camera only achieved 93.0% surface coverage of the EB-PBF sample, where the multi-view method was able to cover 98.7%.

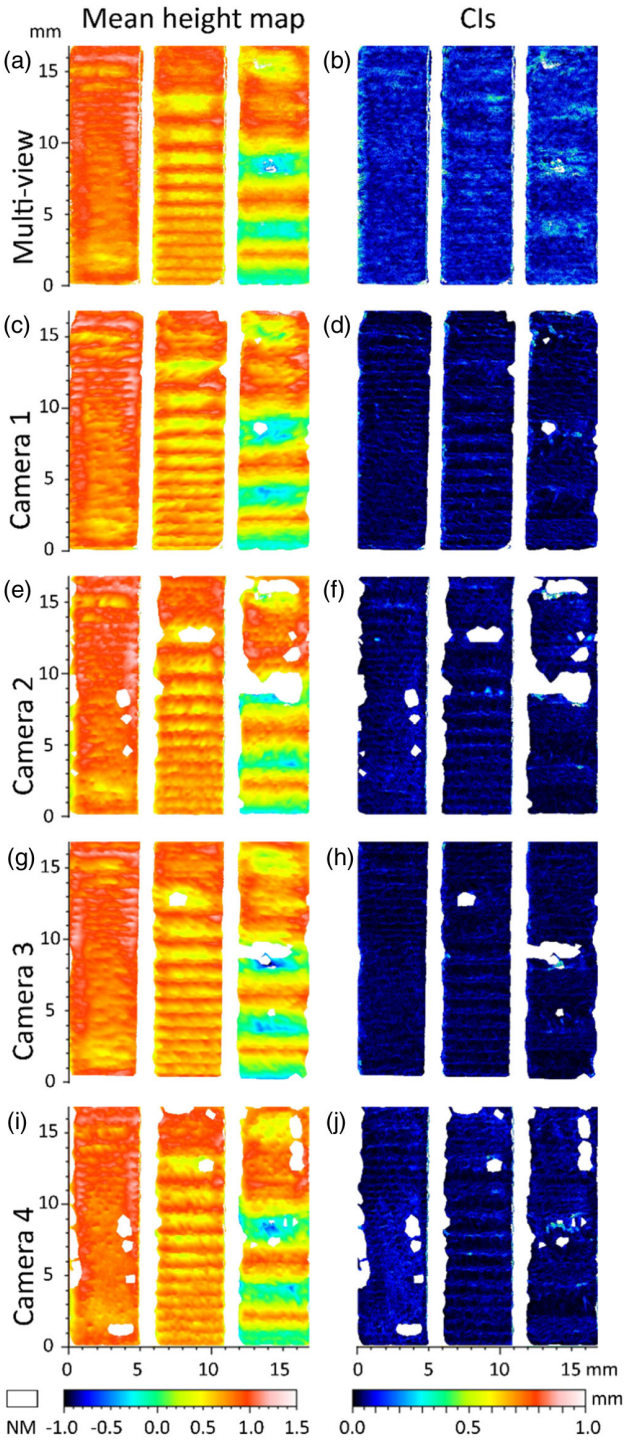

Fig. 7. Mean height maps and CI maps for the (a),(b) multi-view and (c)–(j) single-view fringe projection measurements of the EB-PBF. Single-view fringe projection measurements all show larger regions of data dropout than the multi-view measurements, although CI widths are shown to have increased in the multi-view data.

2. Measurement Performance

CI widths for the fringe projection measurements are presented alongside the height maps in Figs. 7 and 8, while the mean CI

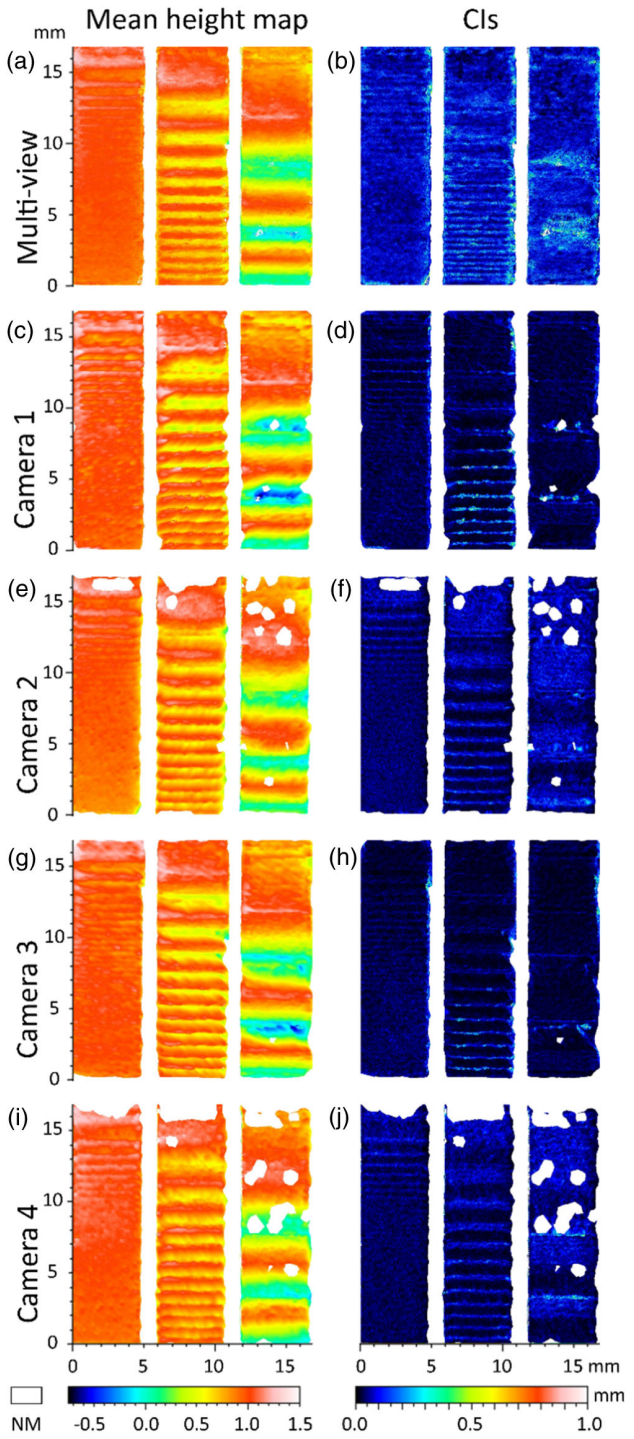

Fig. 8. Mean height maps and CI maps for the (a),(b) multi-view and (c)–(j) single-view fringe projection measurements of the L-PBF. Single-view fringe projection measurements all show larger regions of data dropout than the multi-view measurements, although CI widths are shown to have increased in the multi-view data. The high spatial frequency structured sections of the L-PBF sample that can be seen in the FV data [Fig. 6(c)] were not resolved by either of the fringe projection methods.

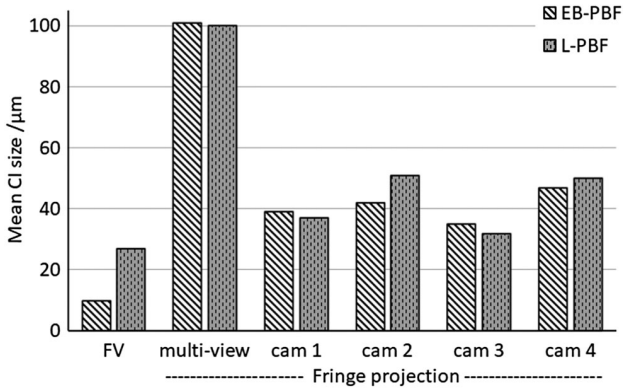

Fig. 9. Mean CI widths for all measurement methods on both the EB-PBF and L-PBF samples.

widths from each measurement are plotted in Fig. 9. The multi-view method is shown to have significantly higher CI widths than each of the single-view height maps. As the same raw point cloud is used in both the single- and multi-view scenarios, the increase in multi-view CI width is not related to the repeatability of the individual camera measurements. Possible reasons for the increase in CI widths when using the multi-view system could be related to the use of data fusion with the multi-view dataset, with errors in the geometric characterization of the global reference frame and the fine alignment performed in Polyworks|Inspector propagating into the final result. Another reason for increased CI widths when using the multi-view could be because the different camera views are effectively measuring different surfaces, since there is a large angular shift between their perspectives. Improvements to the data fusion method could potentially reduce the size of the CI for the multi-view data by reducing relative deformations in the individual point clouds. Although the additional transformations that occur from the data fusion process of the multi-view data introduce further variation, effective averaging from multiple views results in a lower mean deviation than with the single-view height maps, with the mean deviation over both samples for the multi-view system being 68 µm and the mean over all individual views being 84 µm. Mean deviations across the surface for each dataset are presented in Tables 2 and 3.

Deviation maps of the fringe projection datasets against the FV reference are presented in Figs. 10 and 11, along with the corresponding discrepancy maps. Discrepancy (defined in Section 2.C.3) as a percentage of the FV surface is also provided in Tables 2 and 3. The single-view fringe projection height maps each have a much higher discrepancy percentage than the multi-view height maps, with the two multi-view datasets having a mean of 50.5% discrepancy between the two samples and the single-view counter parts having a mean of 78.9% across both samples and all views. The mean deviation across the whole surface is also 16 µm less on average when using the multi-view approach over the single-view measurements (values presented in Tables 2 and 3), which can be seen over the deviation maps presented in Figs. 10 and 11. The reduction in both discrepancies and mean deviations suggests that the multi-view approach has a higher level of accuracy than a single-view system for the same FoV. However, it is worth noting that both the size of the CI widths and the point-by-point deviations will have impacted the discrepancy values. The trade-off between achieving a lower mean deviation

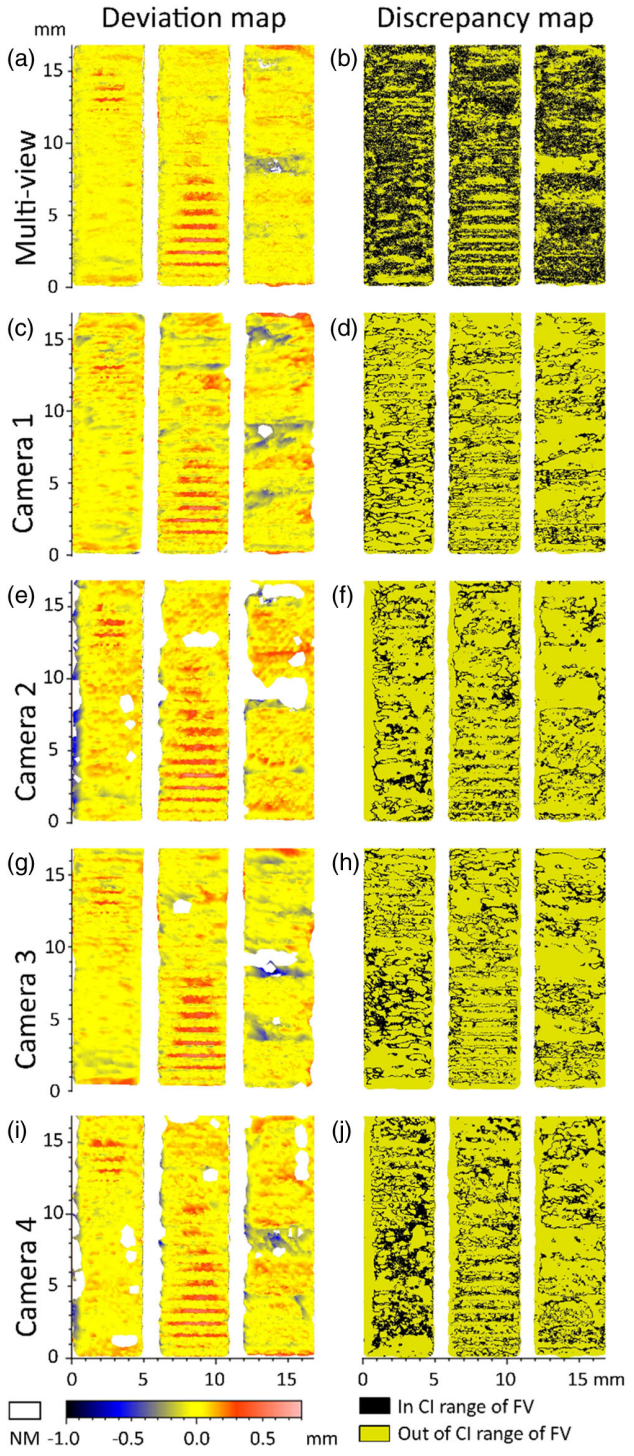

Fig. 10. EB-PBF fringe projection against fringe projection difference map and discrepancy (within CIs). Regions of data dropout from the fringe projection system have been plotted as discrepancies. The multi-view measurement shows a vast improvement in both the deviations and discrepancy across the surface. Each of the single-view fringe projection measurements has significant regions of the surface exceeding 0.5 mm of deviation from the FV measurement that are not present on the multi-view data.

but a higher CI width results in a multi-view system having a higher level of accuracy, but a lower level of precision when compared to the single-view setup.

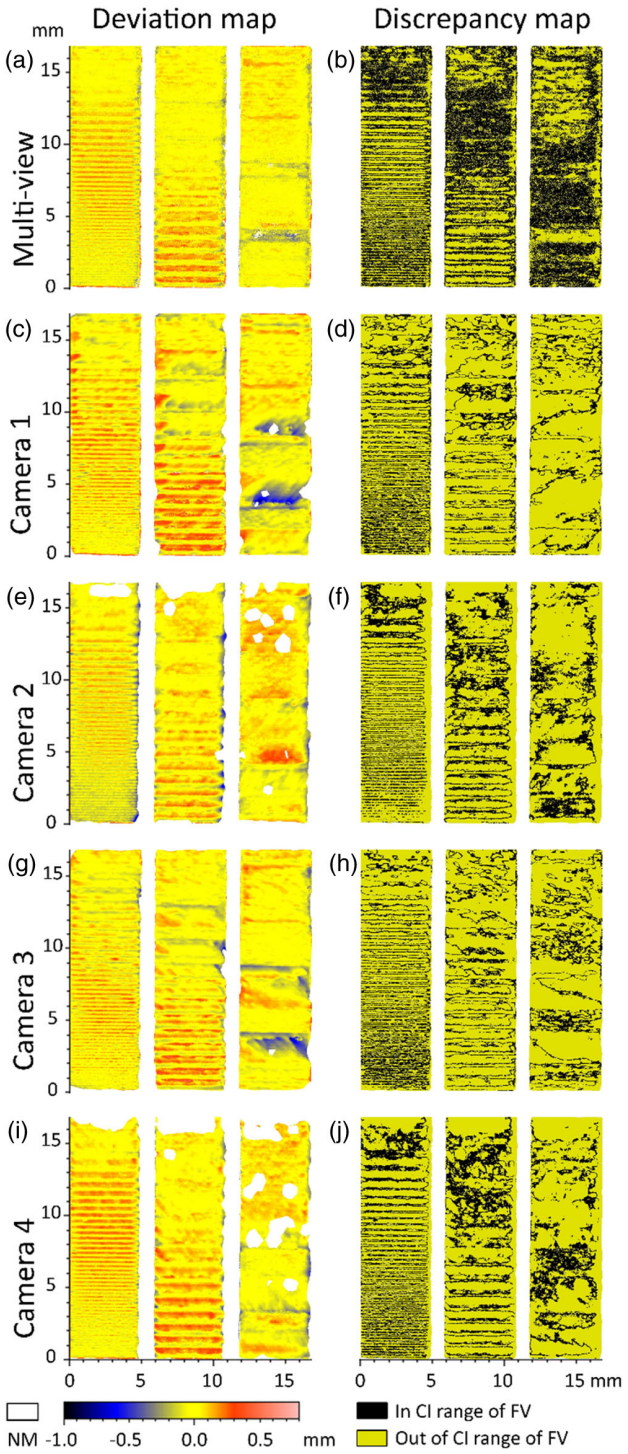

Fig. 11. L-PBF fringe projection against fringe projection difference map and discrepancy (within CIs). Regions of data dropout from the fringe projection system have been plotted as discrepancies. The multi-view measurement shows a vast improvement in both the deviations and discrepancy across the surface. Each of the single-view fringe projection measurements has significant regions of the surface exceeding 0.5 mm of deviation from the FV measurement that are not present on the multi-view data.

A notable contributor to the deviations between the fringe projection and FV data can be observed from the measurements of the deep, narrow valleys present on the L-PBF sample's higher spatial frequency section. The FV measurement of the L-PBF sample presented in Fig. 6(c) shows the high spatial frequency form of section 3. In Fig. 8, none of the fringe projection measurements have been able to resolve the L-PBF samples surface features over the majority of section 3. While the FV system measured the sample orthogonally to the top surface, the cameras of the fringe projection system were viewing the sample from a significant angular offset [seen in Fig. 2(b)], which is a practical necessity for both the fringe projection method and the space limitations within a PBF build chamber. This large angular offset results in the bottom of the sample valleys for the shorter peak-to-peak regions being occluded from the camera's line of sight, meaning that the bottoms of these valleys could not be measured by the fringe projection system, which results in the data showing what appears to be a flat surface across the peaks of the features. A fringe projection system that used a smaller angular offset between the camera and projector would be capable of measuring these valleys if the sample were orientated appropriately. However, within the spatial limits of a PBF system the ability to optimize camera and projector positioning for each sample/build is not possible and therefore these limitations are a result of the fixed hardware positions on this system. Although for the sample used in this paper this appears as a significant limitation of the fringe projection system, for the application of in-process monitoring it would not be expected that repeated features of such a high aspect ratio would occur, as by comparison the powder bed in a PBF is relatively flat.

3. *Point Cloud Density*

The multi-view fringe projection point cloud (pre-meshing and raster scanning) has a mean point spacing of 73.4 μm, with the single camera approach having 136.7 μm (values for each dataset presented in Tables 4 and 5), resulting in a point density that is 3.5 times higher when using the multi-view approach over an area measurement. Although a higher point cloud density does not necessarily translate to a higher spatial resolution, it is a contributing factor that could result in an improved resolution capability in terms of observable features across the PBF layer. However, even with the multi-view setup, the average point spacing of 74.3 μm achieved across the surface will likely need to be reduced further if smaller-scale additive defects are to be detected. Metal PBF defects, such as elongated

Table 4. Mean Point Spacing of the Fringe Projection Point Clouds for the EB-PBF Sample (Rounded to the Nearest Micrometer)

EB-PBF Dataset	Multi-View Fringe Projection/μm	Single-View Fringe Projection/μm			
		Cam1	Cam2	Cam3	Cam4
Repeat 1	76	138	131	158	133
Repeat 2	76	137	131	158	132
Repeat 3	75	137	131	159	131
Repeat 4	76	137	132	158	132
Repeat 5	76	137	131	158	131

Table 5. Mean Point Spacing of the Fringe Projection Point Clouds for the L-PBF Sample (Rounded to the Nearest Micrometer)

L-PBF Dataset	Multi-View Fringe Projection/μm	Single-View Fringe Projection/μm			
		Cam1	Cam2	Cam3	Cam4
Repeat 1	73	147	121	140	129
Repeat 2	72	147	121	141	129
Repeat 3	73	148	123	141	129
Repeat 4	73	147	123	141	129
Repeat 5	73	147	121	142	129

pores (typical size: 50 μm to 500 μm) and unfused powder (typical size: 100 μm to 150 μm) are large enough for multiple points to cover the feature at the achieved point cloud density; however, other defects, such as gas pores (typical size: 5 μm to 20 μm), would not be detected [11].

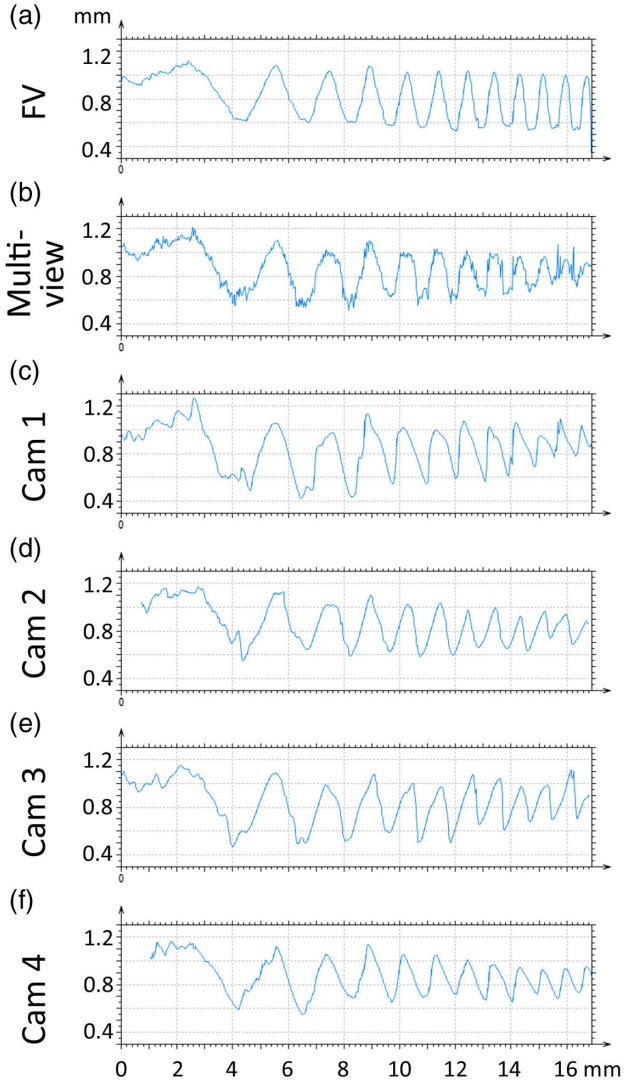

Fig. 12. Line profiles from the aligned datasets of the L-PBF sample. The profile is taken down the approximately the center of section 2 [labeled in Fig. 3(a)].

4. Profiles

Profiles of section 2 for the L-PBF sample are presented in Fig. 12. In the plots, the angular perspectives of the different cameras on the single-camera fringe projection data have clearly influenced the topographies measured. On all single-view measurements, the profile skews in the direction of the camera's placement in the chamber [shown in Fig. 2(b)], with cameras 1 and 4 skewing to the left, and cameras 2 and 3 to the right. This deformation is averaged out in the multi-view data, creating a profile that is more representative of the FV profiles but with a higher level of noise introduced from the fusion process. This skewing effect on single-view fringe projection measurements is a further example of how the single-view approach has a lower level of accuracy than the multi-view approach. The inaccuracies of the single-view measurements over the surface features presents another possible cause for the increase in CI width observed on the multi-view dataset, as the fusion of the multi-view data is effectively averaging out the imperfections of the single-view measurements. This same effect was observed on profiles for all three sections on both samples. The skewing effects of the profiles would be expected to be greatly reduced when performing in-process measurements due to the relative flatness of the powder bed in comparison to the features present on the samples used in this study.

4. CONCLUSIONS

Measurements of two AMSA4 [68] samples, one manufactured through L-PBF and the other EB-PBF, have been performed using a multi-view fringe projection method, single-view fringe projection, and FV to assess the improvements in performance of the multi-view system when compared to single-view data. Measurements made using the multi-view approach provided a reduction in regions of missing data as well as an overall higher point cloud density than the data acquired using a single-view method. In comparison with FV measurements of the same surfaces, the multi-view measurements were shown to be more accurate than a single-view fringe projection measurement, with an average decrease in point-by-point deviations of 16 μm. The multi-view measurements also consistently achieved a higher level of surface coverage, measuring 98.7% and 99.5% of the EB-PBF and the L-PBF surfaces, respectively, as well as a point cloud density 3.5 times higher than the single-view approach. However, although the multi-view system is of higher accuracy, surface coverage, and point density, the data acquired also proved to have a higher average CI width across the measured surface, suggesting a lower level of precision. There are several potential reasons for this increase in CI width, including additional errors introduced by the geometrical characterization and data fusion of the multi-view approach. The individual camera measurements also proved to have a skewing of the high aspect ratio surface features which contributed to the single-view method's decrease in accuracy that was averaged out in the multi-view data for a trade-off of increased noise in these regions.

In the setup that was used for the measurements presented in this paper, the measurement capabilities may not be sufficient for the detection of smaller surface defects that may be present

in the metal PBF build process (sub-100 μm in lateral size). However, modifications could be made to the system to increase point cloud density so that layer-wise defects in the PBF process would be more likely to be detected. With the setup used in this work, each perspective's horizontal FoV was approximately 350 mm. Typical commercial metal PBF systems have a build area between 100 mm and 250 mm in width, meaning that a reduction in camera FoV would still cover the majority, if not all, of the powder bed. Reducing the FoV would result in a higher point density when using the same camera sensor. An alternative way to achieve a higher point cloud density would be to use a higher-resolution camera over the same FoV, or a combination of a higher resolution and a lower FoV that is best suited to the AM system's chamber dimensions.

A. Future Work

To improve the performance of the system presented, modifications will be made including improvements to the geometric characterization method and the use of a higher specification industrial projector to improve projection stability. Further testing will also be performed with the cameras configured to cover a smaller measurement area to further increase the point cloud density, making the system better suited for the detection of smaller-scale PBF defects.

The current system's acquisition time for the 19 total images captured would be too long to realistically be used as an in-process measurement tool without significantly increasing the build time of a part. The limiting factor stopping the system from measuring at a faster rate is the use of a commercial projector that cannot be hardware synchronized with the cameras. In theory, when using an industrial projector the acquisition rate would be limited by the camera's maximum frame rate of 17 fps, which would result in the 19 images being captured just over 1 s. The acquisition time could then be reduced further by using higher framerate cameras if necessary.

The data processing pipeline described in this paper includes multiple manual stages to achieve the multi-view point cloud. Future versions of the fringe projection software will include automatic fusion between the four separate point clouds to provide a single measurement output. Processing times of the multi-view phase unwrapping and point cloud fusion will be of great importance for in-process application and will be assessed accordingly.

Future testing of the system's capabilities will include feature-based segmentation [60–63] of the multi-view fringe projection measurements to assess how well metal PBF surface features can be identified using this approach. The multi-view system is now being commercialized by Taraz Metrology Ltd. and will be tested in several commercial PBF systems.

Funding. Engineering and Physical Sciences Research Council (grant EP/P021468/1).

Acknowledgment. The authors would like to acknowledge the support of the EPSRC for funding this work, Dr. Lewis Newton (University of Nottingham) for his expertise in performing FV measurements, Sofia Catalucci (University of Nottingham) for her expertise and guidance in the use of the Polyworks and CloudCompare software, and Julien Hennequez (National Engineering School of Saint-Etienne) for aid in the construction and testing of the multi-view fringe projection system.

Disclosures. The authors declare no conflicts of interest.

REFERENCES

1. I. Campbell, O. Diegel, R. Huff, J. Kowen, T. Wohlers, D. Bourell, I. Fidan, and P. Sander, "Wohlers Report 2020: 3D Printing and Additive Manufacturing State of the Industry" (Wohlers Associates, 2020).
2. W. Gao, H. Haitjema, F. Z. Fang, R. K. Leach, C. F. Cheung, E. Savio, and J. M. Linares, "On-machine and in-process surface metrology for precision manufacturing," CIRP Ann. **68**, 843–866 (2019).
3. R. K. Leach, D. Bourell, S. Carmignato, A. Donmez, N. Senin, and W. Dewulf, "Geometrical metrology for metal additive manufacturing," CIRP Ann. **68**, 677–700 (2019).
4. P. Bidare, R. R. J. Maier, R. J. Beck, J. D. Shephard, and A. J. Moore, "An open-architecture metal powder bed fusion system for in-situ process measurements," Addit. Manuf. **16**, 177–185 (2017).
5. C. L. A. Leung, S. Marussi, R. C. Atwood, M. Towrie, P. J. Withers, and P. D. Lee, "In situ X-ray imaging of defect and molten pool dynamics in laser additive manufacturing," Nat. Commun. **9**, 1355 (2018).
6. C. Zhao, K. Fezzaa, R. W. Cunningham, H. Wen, F. De Carlo, L. Chen, A. D. Rollett, and T. Sun, "Real-time monitoring of laser powder bed fusion process using high-speed X-ray imaging and diffraction," Sci. Rep. **7**, 3602 (2017).
7. W. E. Frazier, "Metal additive manufacturing: a review," J. Mater. Eng. Perform. **23**, 1917–1928 (2014).
8. I. Gibson, D. Rosen, and B. Stucker, *Additive Manufacturing Technologies: 3D Printing, Rapid Prototyping, and Direct Digital Manufacturing*, 2nd ed. (Springer, 2015).
9. G. N. Levy, R. Schindel, and J. P. Kruth, "Rapid manufacturing and rapid tooling with layer manufacturing (LM) technologies, state of the art and future perspectives," CIRP Ann. **52**, 589–609 (2003).
10. B. M. Lane, S. Mekhontsev, S. E. Grantham, M. Vlasea, J. G. Whiting, H. Yeung, J. C. Fox, C. J. Zarobila, J. E. Neira, M. L. McGlauflin, L. M. Hanssen, S. P. Moylan, M. A. Donmez, and J. P. Rice, "Design, developments, and results from the NIST Additive Manufacturing Metrology Testbed (AMMT)," in *Solid Freeform Fabrication (SFF) Symposium* (2016), pp. 1145–1160.
11. S. K. Everton, M. Hirsch, P. Stravroulakis, R. K. Leach, and A. T. Clare, "Review of in-situ process monitoring and in-situ metrology for metal additive manufacturing," Mater. Des. **95**, 431–445 (2016).
12. M. Mani, B. M. Lane, M. A. Donmez, S. C. Feng, and S. P. Moylan, "A review on measurement science needs for real-time control of additive manufacturing metal powder bed fusion processes," Int. J. Prod. Res. **55**, 1400–1418 (2017).
13. M. Grasso and B. M. Colosimo, "Process defects and in situ monitoring methods in metal powder bed fusion: a review," Meas. Sci. Technol. **28**, 044005 (2017).
14. S. Berumen, F. Bechmann, S. Lindner, J.-P. Kruth, and T. Craeghs, "Quality control of laser- and powder bed-based additive manufacturing (AM) technologies," Phys. Procedia **5**, 617–622 (2010).
15. A. Gökhan Demir, C. De Giorgi, and B. Previtali, "Design and implementation of a multisensor coaxial monitoring system with correction strategies for selective laser melting of a maraging steel," J. Manuf. Sci. Eng. **140**, 041003 (2018).
16. B. M. Lane, S. E. Grantham, H. Yeung, C. J. Zarobila, and J. C. Fox, "Performance characterization of process monitoring sensors on the NIST Additive Manufacturing Metrology Testbed," in *Solid Freeform Fabrication (SFF) Symposium* (2017).
17. S. E. Grantham, B. M. Lane, J. E. Neira, S. Mekhontsev, L. M. Hanssen, and M. Vlasea, "Optical design and initial results from NIST's AMMT/TEMPS facility," Proc. SPIE **9738**, 97380S (2016).
18. V. Renken, A. von Freyberg, K. Schünemann, F. Pastors, and A. Fischer, "In-process closed-loop control for stabilising the melt

pool temperature in selective laser melting," Prog. Addit. Manuf. **4**, 411–421 (2019).
19. B. Yuan, B. Giera, G. Guss, I. Matthews, and S. McMains, "Semi-supervised convolutional neural networks for in-situ video monitoring of selective laser melting," in *IEEE Winter Conference on Applications of Computer Vision (WACV)* (2019).
20. I. A. Okaro, S. Jayasinghe, C. Sutcliffe, K. Black, P. Paoletti, and P. L. Green, "Automatic fault detection for laser powder-bed fusion using semi-supervised machine learning," Addit. Manuf. **27**, 42–53 (2019).
21. A. J. Manzo and H. Helvajian, "Utility of optical heterodyne displacement sensing and laser ultrasonics as in situ process control diagnostic for additive manufacturing," Opt. Eng. **57**, 041415 (2018).
22. O. Kwon, H. G. Kim, M. J. Ham, W. Kim, G.-H. Kim, J.-H. Cho, N. I. Kim, and K. Kim, "A deep neural network for classification of melt-pool images in metal additive manufacturing," J. Intell. Manuf. **31**, 375–386 (2020).
23. T. Craeghs, S. Clijsters, E. Yasa, and J.-P. Kruth, "Online quality control of selective laser melting," in *Solid Freeform Fabrication (SFF) Symposium* (2011).
24. B. Zhang, S. Liu, and Y. C. Shin, "In-process monitoring of porosity during laser additive manufacturing process," Addit. Manuf. **28**, 497–505 (2019).
25. P. Earle, "Quality assurance: Is data from in-situ monitoring similar to a CT scan?" in *Additive Manufacturing Users Group Conference* (2017).
26. M. Khanzadeh, S. Chowdhury, M. Marufuzzaman, M. A. Tschopp, and L. Bian, "Porosity prediction: supervised-learning of thermal history for direct laser deposition," J. Manuf. Syst. **47**, 69–82 (2018).
27. G. Mohr, S. J. Altenburg, A. Ulbricht, P. Heinrich, D. Baum, C. Maierhofer, and K. Hilgenberg, "In-situ defect detection in laser powder bed fusion by using thermography and optical tomography–comparison to computed tomography," Metals **10**, 103 (2020).
28. L. Song, F. Wang, S. Li, and X. Han, "Phase congruency melt pool edge extraction for laser additive manufacturing," J. Mater. Process. Technol. **250**, 261–269 (2017).
29. T. Furumoto, M. R. Alkahari, T. Ueda, M. S. A. Aziz, and A. Hosokawa, "Monitoring of laser consolidation process of metal powder with high speed video camera," Phys. Procedia **39**, 760–766 (2012).
30. G. Repossini, V. Laguzza, M. Grasso, and B. M. Colosimo, "On the use of spatter signature for in-situ monitoring of laser powder bed fusion," Addit. Manuf. **16**, 35–48 (2017).
31. N. Boone, C. Zhu, C. Smith, I. Todd, and J. R. Willmott, "Thermal near infrared monitoring system for electron beam melting with emissivity tracking," Addit. Manuf. **22**, 601–605 (2018).
32. E. Rodriguez, F. Medina, D. Espalin, C. A. Terrazas, D. Muse, C. Henry, E. MacDonald, and R. B. Wicker, "Integration of a thermal imaging feedback control system in electron beam melting," in *Solid Freeform Fabrication (SFF) Symposium* (2012).
33. H. Krauss, T. Zeugner, and M. F. Zaeh, "Layerwise monitoring of the selective laser melting process by thermography," Phys. Procedia **56**, 64–71 (2014).
34. J. Z. Jacobsmuhlen, G. Witt, S. Kleszczynski, and D. Merhof, "Elevated region area measurement for quantitative analysis of laser beam melting process stability," in *Solid Freeform Fabrication (SFF) Symposium* (2015).
35. F. Caltanissetta, M. Grasso, S. Petrò, and B. M. Colosimo, "Characterization of in-situ measurements based on layerwise imaging in laser powder bed fusion," Addit. Manuf. **24**, 183–199 (2018).
36. C. Gobert, E. W. Reutzel, J. Petrich, A. R. Nassar, and S. Phoha, "Application of supervised machine learning for defect detection during metallic powder bed fusion additive manufacturing using high resolution imaging," Addit. Manuf. **21**, 517–528 (2018).
37. L. Scime and J. Beuth, "A multi-scale convolutional neural network for autonomous anomaly detection and classification in a laser powder bed fusion additive manufacturing process," Addit. Manuf. **24**, 273–286 (2018).
38. C. Barrett, E. MacDonald, B. Conner, and F. Persi, "Micron-level layer-wise surface profilometry to detect porosity defects in powder bed fusion of Inconel 718," J. Miner. Metals Mater. Soc. **70**, 1844–1852 (2018).
39. L. Tan Phuc and M. Seita, "A high-resolution and large field-of-view scanner for in-line characterization of powder bed defects during additive manufacturing," Mater. Des. **164**, 107562 (2019).
40. W. S. Land, B. Zhang, J. Ziegert, and A. Davies, "In-situ metrology system for laser powder bed fusion additive process," Procedia Manuf. **1**, 393–403 (2015).
41. B. Zhang, W. S. Land, J. Ziegert, and A. Davies, "In situ monitoring of laser powder bed fusion additive manufacturing using digital fringe projection technique," in *ASPE 2015 Spring Topical Meeting* (2015).
42. B. Zhang, J. Ziegert, F. Farahi, and A. Davies, "In situ surface topography of laser powder bed fusion using fringe projection," Addit. Manuf. **12**, 100–107 (2016).
43. Z. Li, X. Liu, S. Wen, P. He, K. Zhong, Q. Wei, Y. Shi, and S. Liu, "In situ 3D monitoring of geometric signatures in the powder-bed-fusion additive manufacturing process via vision sensing methods," Sensors **18**, 1180 (2018).
44. N. Southon, P. Stavroulakis, R. Goodridge, and R. Leach, "In-process measurement and monitoring of a polymer laser sintering powder bed with fringe projection," Mater. Des. **157**, 227–234 (2018).
45. Y. Liu, Z. Zhang, L. Blunt, G. Saunby, J. Dawes, B. Blackham, H. A. Rahman, C. Smith, F. Gao, and X. Jiang, "In-situ areal inspection of powder bed for electron beam fusion AM system based on fringe projection," in *ASPE and EUSPEN Summer Topical Meeting* (2018), pp. 259–264.
46. Y. Liu, L. Blunt, Z. Zhang, H. A. Rahman, F. Gao, and X. Jiang, "In-situ areal inspection of powder bed for electron beam fusion system based on fringe projection profilometry," Addit. Manuf. **31**, 100940 (2020).
47. H. Nguyen, D. Nguyen, Z. Wang, H. Kieu, and M. Le, "Real-time, high-accuracy 3D imaging and shape measurement," Appl. Opt. **54**, A9–A17 (2015).
48. C. Jiang, S. Jia, J. Dong, Q. Bao, J. Yang, Q. Lian, and D. Li, "Multi-frequency color-marked fringe projection profilometry for fast 3D shape measurement of complex objects," Opt. Express **23**, 24152–24162 (2015).
49. S. Zhang, "High-speed 3D shape measurement with structured light methods: a review," Opt. Lasers Eng. **106**, 119–131 (2018).
50. P. I. Stavroulakis and R. K. Leach, "Invited review article: review of post-process optical form metrology for industrial-grade metal additive manufactured parts," Rev. Sci. Instrum. **87**, 041101 (2016).
51. J. B. Pawley, "Points, pixels, and gray levels: digitizing image data," in *Handbook of Biological Confocal Microscopy*, J. B. Pawley, ed. (Springer, 2006), pp. 59–79.
52. L. Song, Y. Gao, X. Zhu, Q. Guo, and J. Xi, "A 3D measurement method based on multi-view fringe projection by using a turntable," Optoelectron. Lett. **12**, 389–394 (2016).
53. R. Ernst, A. Weckenmann, and R. Velgan, "Local wall thickness measurement of formed sheet metal using fringe projection technique," in *XVII IMEKO World Congress* (2003).
54. K. Genovese and C. Pappalettere, "Whole 3D shape reconstruction of vascular segments under pressure via fringe projection techniques," Opt. Laser. Eng. **44**, 1311–1323 (2006).
55. H. Du, X. Chen, J. Xi, C. Yu, and B. Zhao, "Development and verification of a novel robot-integrated fringe projection 3D scanning system for large-scale metrology," Sensors **17**, 2886 (2017).
56. M. Rao, D. Radhakrishna, and S. Usha, "Development of a robot-mounted 3D scanner and multi-view registration techniques for industrial applications," Procedia Comput. Sci. **133**, 256–267 (2018).
57. M. Wang, Y. Yin, D. Deng, X. Meng, X. Liu, and X. Peng, "Improved performance of multi-view fringe projection 3D microscopy," Opt. Express **25**, 19408–19421 (2017).
58. A. Shaheen, D. Sims-Waterhouse, P. Bointon, S. Piano, and R. Leach, "Automated characterisation of multi-view fringe projection system for three- dimensional measurement of additively manufactured parts," in *ASPE and euspen Summer Topical Meeting on Advancing Precision in Additive Manufacturing* (2019).
59. M. Gdeisat, M. Qudeisat, M. AlSa'd, D. Burton, F. Lilley, and M. M. M. Ammous, "Simple and accurate empirical absolute volume calibration of a multi-sensor fringe projection system," Opt. Lasers Eng. **80**, 32–44 (2016).

60. L. Newton, N. Senin, B. Smith, E. Chatzivagiannis, and R. K. Leach, "Comparison and validation of topography segmentation methods for feature-based characterisation of metal powder bed fusion surfaces," Surf. Topogr. Metrol. Prop. **7**, 045020 (2019).
61. S. Lou, X. Jiang, W. Sun, W. Zeng, L. Pagani, and P. J. Scott, "Characterisation methods for powder bed fusion processed surface topography," Precis. Eng. **57**, 1–15 (2019).
62. N. Senin, A. Thompson, and R. Leach, "Feature-based characterisation of signature topography in laser powder bed fusion of metals," Meas. Sci. Technol. **29**, 045009 (2018).
63. S. Lou, L. Pagani, W. Zeng, X. Jiang, and P. J. Scott, "Watershed segmentation of topographical features on freeform surfaces and its application to additively manufactured surfaces," Precis. Eng. **63**, 177–186 (2020).
64. A. Dickins, T. Widjanarko, S. Lawes, P. Stavroulakis, and R. Leach, "Design of a multi-sensor in-situ inspection system for additive manufacturing," in *ASPE and EUSPEN Summer Topical Meeting on Advancing Precision in Additive Manufacturing* (2018).
65. F. Helmi, "Focus variation instruments," in *Optical Measurement of Surface Topography*, R. K. Leach, ed. (Springer, 2011), pp. 131–166.
66. C. L. Giusca, J. D. Claverley, W. Sun, R. K. Leach, F. Helmli, and M. P. J. Chavigner, "Practical estimation of measurement noise and flatness deviation on focus variation microscopes," CIRP Ann. **63**, 545–548 (2014).
67. A. Alburayt, W. P. Syam, and R. Leach, "Lateral scale calibration for focus variation microscopy," Meas. Sci. Technol. **29**, 065012 (2018).
68. A. Townsend, R. Racasan, and L. Blunt, "Surface-specific additive manufacturing test artefacts," Surf. Topogr. Metrol. Prop. **6**, 024007 (2018).
69. D. C. Girardeau-Montaut, "CloudCompare v2.11 alpha (Anoia) [64 bit]," 2019, https://www.danielgm.net/cc.
70. InnovMetric Software, "Polyworks|InspectorTM 2019 IR2 64-bit (build 2869)," 2019, https://www.innovmetric.com/en/products-solutions/polyworksinspectortm.
71. P. J. Besl and N. D. McKay, "A method for registration of 3-D shapes," IEEE Trans. Pattern Anal. Mach. Intell. **14**, 239–256 (1992).
72. Z. Zhang, "Iterative point matching for registration of free-form curves and surfaces," Int. J. Comput. Vis. **13**, 119–152 (1994).
73. T.-P. Fang and L. A. Piegl, "Delaunay triangulation in three dimensions," IEEE Comput. Graph. **15**, 62–69 (1995).
74. A. Thompson, N. Senin, C. Giusca, and R. Leach, "Topography of selectively laser melted surfaces: a comparison of different measurement methods," CIRP Ann. **66**, 543–546 (2017).
75. N. Senin, A. Thompson, and R. K. Leach, "Characterisation of the topography of metal additive surface features with different measurement technologies," Meas. Sci. Technol. **28**, 095003 (2017).
76. M.-A. de Pastre, A. Thompson, Y. Quinsat, J. A. Albajez, N. Senin, and R. K. Leach, "Polymer powder bed fusion surface texture measurement," Meas. Sci. Technol. **31**, 055002 (2020).
77. Digital Surf, "MountainsMap® Premium v7.4.9053," 2019, https://www.digitalsurf.com/.
78. L. Newton, N. Senin, C. Gomez, R. Danzl, F. Helmli, L. Blunt, and R. Leach, "Areal topography measurement of metal additive surfaces using focus variation microscopy," Addit. Manuf. **25**, 365–389 (2019).